

# Where did heavy binaries go?

## Gravitational-wave populations using Delaunay triangulation with optimized complexity

RODRIGO TENORIO  <sup>1,2</sup> ALEXANDRE TOUBIANA  <sup>1,2</sup> TRISTAN BRUEL  <sup>1,2</sup> DAVIDE GEROSA  <sup>1,2</sup> AND JONATHAN R. GAIR  <sup>3</sup>

<sup>1</sup>*Dipartimento di Fisica “G. Occhialini”, Università degli Studi di Milano-Bicocca, Piazza della Scienza 3, 20126 Milano, Italy*

<sup>2</sup>*INFN, Sezione di Milano-Bicocca, Piazza della Scienza 3, 20126 Milano, Italy*

<sup>3</sup>*Max Planck Institute for Gravitational Physics (Albert Einstein Institute), Am Mühlenberg 1, 14476, Potsdam, Germany*

### ABSTRACT

We investigate the joint mass-redshift evolution of the binary black hole merger rate in the latest gravitational-wave detection catalog, GWTC-4.0. We present and apply a novel non-parametric framework for modeling multi-dimensional, correlated distributions based on Delaunay triangulation. Crucially, the complexity of the model—namely, the number, positions, and weights of triangulation nodes—is inferred directly from the data, resulting in a highly efficient approach that requires about one to two orders of magnitude fewer parameters and significantly less calibration than current state-of-the-art methods. We find no evidence for a peak at  $M_{\text{tot}} \sim 70M_{\odot}$  at low redshifts ( $z \sim 0.2$ ), where it would correspond to the  $m_1 \sim 35M_{\odot}$  feature reported in redshift-independent mass spectrum analyses, and we infer an increased merger rate at high redshifts ( $z \sim 1$ ) around those masses, compatible with such a peak. We discuss the astrophysical implications of these results.

### 1. INTRODUCTION

The increasing number of binary black holes (BBHs) observed by gravitational-wave (GW) interferometers (Abbott et al. 2019, 2021, 2023a, 2024; Abac et al. 2025c) deepens our understanding of their population in the Universe (Abac et al. 2025b), eventually revealing their origin out of the multiple proposed formation channels (Mandel & Farmer 2022; Mapelli 2021). A crucial step in this direction is the identification of correlations between parameters and the presence of distinct subpopulations (e.g. Callister 2024 and references therein)

A key question is whether, and how, the BBH population evolves with redshift and, crucially, whether this evolution depends on the BBH properties. BBHs are the end products of stellar evolution; therefore, their population should depend on the star-formation history and properties of galaxies such as metallicity (Mapelli et al. 2019; Neijssel et al. 2019; van Son et al. 2022b; de Sá et al. 2024; Broekgaarden et al. 2021). Moreover, BBHs involving remnants of previous mergers, formed through dynamical encounters, also contribute to the evolution of the population’s properties (Gerosa & Fishbach 2021; Ye & Fishbach 2024; Torniamenti et al. 2024). Finally, the redshift evolution encodes the relative contribution of

the different BBH formation channels throughout cosmic history (Mapelli et al. 2022; Sedda et al. 2023).

Evidence for an evolution of the effective spin distribution with redshift (Biscoveanu et al. 2022) was found on the third gravitational-wave transient catalog (GWTC-3) by LIGO, Virgo, and KAGRA, and was further strengthened in their fourth catalog (GWTC-4.0; Abac et al. 2025b). In contrast, several analyses of GWTC-3 found no evidence for or against a redshift evolution in the mass distribution (Ray et al. 2023; Heinzel et al. 2025; Sadiq et al. 2025; Lalleman et al. 2025; Gennari et al. 2025), and first analyses on GWTC-4.0 find similar conclusions (Abac et al. 2025b).<sup>1</sup>

In this work, we investigate the joint mass-redshift evolution of the BBH merger rate using a novel non-parametric multi-dimensional approach. In particular, we reconstruct the joint mass-redshift BBH merger rate using Delaunay triangulation (Delaunay 1934) and barycentric interpolation. Both the number and locations of the triangulation vertices, as well as their associated weights, are inferred directly from the data through trans-dimensional Bayesian inference (Toubiana et al. 2023). The use of a data-driven interpolation scheme assumes no specific functional (in)dependence between mass and

Email: rodrigo.tenorio@unimib.it

<sup>1</sup> While Rinaldi et al. (2024) did report evidence for such an evolution, their treatment of selection effects is not accurate (Essick & Fishbach 2024; Toubiana et al. 2025b).

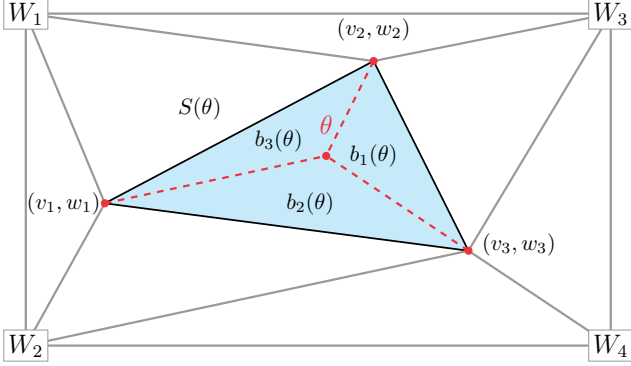


**Figure 1.** Delaunay triangulation and barycentric interpolation to model the log differential merger rate  $\log_{10} d_\theta N$  across two variables (on the horizontal and vertical axes, respectively). The central red dot represents a location  $\theta$  where the rate needs to be computed. The highlighted area  $S(\theta)$  represents the triangle (*simplex* in higher dimensions) containing  $\theta$  whose vertices  $v_i$  and weights  $w_i$  are inferred from the data. The position of the four corners is fixed in advance, and their weights  $W_i$  are inferred from the data. The rate  $\log_{10} d_\theta N$  is computed by interpolating the weights at the vertices of  $S(\theta)$  using the barycentric coordinates  $b_i(\theta)$  associated to  $\theta$ .

redshift; this allows us to probe a broader parameter space compared to models with closed-form correlations.

Using GWTC-4.0 data, we report a distinct difference in the distribution of masses at  $z = 0.2$  and  $z = 1.0$  at  $M_{\text{tot}} \sim 70 M_\odot$ , with no evidence for the presence of a peak in the merger rate at said masses for  $z = 0.2$ . We then discuss the astrophysical implications of our findings.

## 2. MASS-REDSHIFT CORRELATION

We denote the targeted set of source parameters by  $\theta$ , consisting of total mass  $M_{\text{tot}}$ , mass ratio  $q \leq 1$ , redshift  $z$ , spin  $\chi_{1,2}$  and cosine of the spin tilts  $\cos \vartheta_{1,2}$ . To capture potential dependencies between  $M_{\text{tot}}$  and  $z$ , we model the differential number of events  $d_\theta N(\theta|\Lambda)$  as

$$\begin{aligned} \log d_\theta N(\theta|\Lambda) = & \Delta(M_{\text{tot}}, z|\Lambda_\Delta) + \log [p(q|M_{\text{tot}}, \Lambda_q)] \\ & + \log [p(\chi_1|\Lambda_\chi)p(\chi_2|\Lambda_\chi)] + \log [p(\cos \vartheta_1, \cos \vartheta_2|\Lambda_\vartheta)], \end{aligned} \quad (1)$$

where  $\Delta(M_{\text{tot}}, z|\Lambda_\Delta)$  represents the (natural log) differential rate as computed by barycentric interpolation using Delaunay triangulation. The hyperparameters  $\Lambda_\Delta$  are the number of triangulation vertices, their locations, and the value of the differential rate at those vertices. Figure 1 gives a schematic description of our model; further details are provided in Appendix A. The mass ratio distribution is modeled as a broken power-law. For the spin magnitudes and tilt angles we assume the same functional forms as in the default model by Abac et al. (2025b). The hyperparameters  $\Lambda = (\Lambda_\Delta, \Lambda_q, \Lambda_\chi, \Lambda_\vartheta)$  are

inferred through hierarchical Bayesian inference (see Appendix B for details). The differential volumetric rate of GW events is then given by

$$d_\theta \mathcal{R} = \left( \frac{T_{\text{obs}}}{1+z} \frac{dV_c}{dz} \right)^{-1} d_\theta N, \quad (2)$$

where  $T_{\text{obs}}$  is the observation time. For completeness, we denote as  $m_{1,2}$  the primary and secondary masses.

We limit the domain of inference for the  $(M_{\text{tot}}, z)$  distribution to  $[6, 350] M_\odot \times [0, 2.5]$ . Priors on triangulation vertices are uniform within this domain, and weights are uniformly distributed along  $(-20, 15)$ . The number of triangulation nodes is allowed to vary between 4 and 100. We have verified our findings to be robust against the choice of prior. Inference is conducted using reversible-jump Markov chain Monte Carlo as implemented in `eryn` (Karnesis et al. 2023).

The triangulation scheme that best fits the  $(M_{\text{tot}}, z)$  portion of the population has  $17^{+25}_{-11}$  nodes, corresponding to  $56^{+75}_{-33}$  free parameters (90% credible interval). This is one to two orders of magnitude fewer than those needed by Heinzel et al. (2025), and requires significantly less tuning compared to Ray et al. (2023). Crucially, both those approaches rely on a fixed two-dimensional grid and are therefore expected to scale poorly with the number of dimensions, whereas Delaunay triangulation is naturally applicable to higher-dimensional correlations (Toubiana et al. 2025a).

The left panel of Fig. 2 shows our reconstructed volumetric differential rate at two representative redshift values ( $z = 0.2$  and  $z = 1.0$ ). Their behavior is different:

- At  $z = 0.2$ , the merger rate shows a distinctive peak at  $M_{\text{tot}} \sim 20 M_\odot$  and decays in a featureless, power-law-like manner.
- For  $z = 1$ , the merger rate increases with respect to that at low redshifts for  $M_{\text{tot}} \sim 70 M_\odot$  and appears to peak at those masses.

The right panel of Fig. 2 quantifies the credibility of the  $z \sim 1$ ,  $M_{\text{tot}} \sim 70$  feature at 98.5%. That is,  $d_\theta \mathcal{R}(z=1) > d_\theta \mathcal{R}(z=0.2)$  at a least one value of  $M_{\text{tot}}$  for 98.5% of the posterior volumetric rate. Said increase with redshift is compatible with that found by Abac et al. (2025c) using a mass-independent power-law model.

While we cannot definitively claim that the mass distribution at  $z = 1.0$  exhibits a peak at  $70 M_\odot$  owing to the error bars, a corresponding feature at  $m_1 \sim 35 M_\odot$  has been consistently identified since GWTC-2 (Abbott et al. 2021). Our findings suggest that this feature is associated with high-redshift BBHs and disappears by  $z = 0.2$ . In Appendix C, we show the results of applying

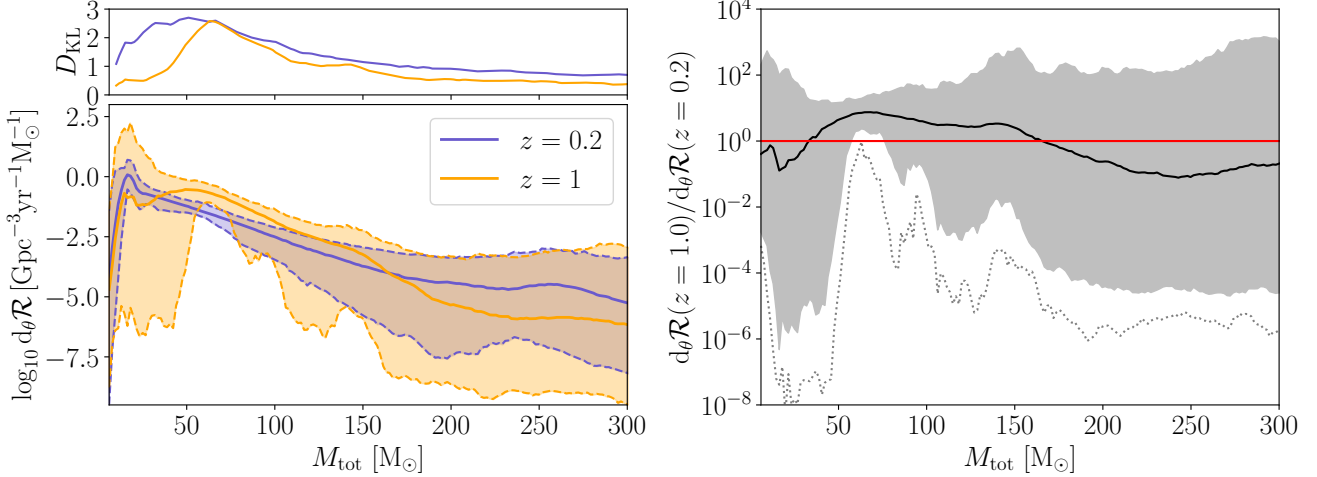


**Figure 2.** *Left:* Volumetric differential rate reconstructed using Delaunay triangulation for two representative redshift values,  $z = 0.2$  (purple) and  $z = 1$  (orange). Solid curves indicate the medians while shaded regions encompass 90% symmetric credible intervals. The upper panel shows the Kullback-Leibler divergence between the posterior and prior volumetric differential rate distributions. *Right:* Ratio of the volumetric differential rate at the same two representative redshift values. The black solid curve denotes the posterior median. The shaded region contains the symmetric 90% credible interval. The horizontal red line corresponds to  $d_\theta \mathcal{R}(z = 0.2) = d_\theta \mathcal{R}(z = 1)$ . The dotted line corresponds to the 1.5% credibility interval. The observed difference in rates is thus inconsistent with no evolution of the rate with  $z$  at 98.5% credibility, but remains consistent with a mass-uniform evolution (the envelope is consistent with a straight line).

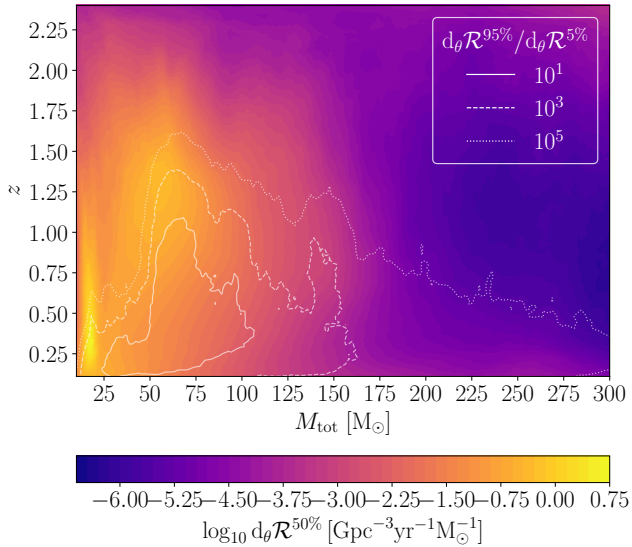


**Figure 3.** The color scale shows the median (50% quantile) posterior volumetric rate inferred using Delaunay triangulation on GWTC-4.0. The white contours indicate the relative uncertainty on the rate itself, defined as the ratio between the 95% quantile and the 5% quantile.

our method to  $(m_1, z)$  and illustrate how our discussion of the  $70 M_\odot$  feature similarly applies to the  $35 M_\odot$  peak in  $m_1$ . Our inference on the mass-ratio distribution is consistent with a larger density at  $q \gtrsim 0.6$ , similarly to what reported by Abac et al. (2025b).

Figure 3 presents the outcome of our inference across the  $(M_{\text{tot}}, z)$  parameter space. We find that BBHs with different masses merge more prominently at different redshifts and that the high-mass prominence appears around  $z \sim 0.7$ . However, given current uncertainties, no definitive statement about distinct BBH sub-populations can yet be made. The region of high uncertainty roughly aligns with the detection horizon beyond which no BBH mergers were detected.

We also infer a peak in the merger rate at  $M_{\text{tot}} \sim 20 M_\odot$  for  $z = 0.2$ , but the lack of detections at higher redshifts prevents us from confirming or disproving its existence for  $z \gtrsim 0.2$ .

Our findings are not sufficient to establish whether the mass distribution changes with redshift, as the relative difference in rates is consistent with a mass-independent rescaling (see right panel of Fig. 2). The key result of this letter is the disappearance of the high-mass peak at low redshift.

We characterize the high-redshift appearance of the  $70 M_\odot$  peak by computing Kullback-Leibler divergence ( $D_{\text{KL}}$ ) (Kullback & Leibler 1951) between the posterior and the prior on the rate induced by our prior on  $\Lambda_\Delta$ . For reference,  $D_{\text{KL}} \lesssim 0.1$  between two independent prior draws. As shown in the upper left panel of Fig. 2, we find significantly larger values  $D_{\text{KL}} \sim 2.5$  around  $M_{\text{tot}} \sim 70 M_\odot$ , showing that these results are primarily driven by the observed data.

Altogether, these results indicate that the known feature in the BBH mass distribution (Abbott et al. 2021,

2023b; Abac et al. 2025b) varies with redshift. Future analyses should consider targeting such behaviour with modeled approaches.

Our results differs from those by Abac et al. (2025b), which reported no evidence for a mass-dependent redshift evolution of the merger rate using both copulas (Adamcewicz & Thrane 2022) and binned Gaussian processes (Ray et al. 2023). Copulas are suited to capture simple correlations, as opposed to the structures inferred in Fig. 3. In the binned Gaussian process approach, the high-mass feature appears less pronounced at lower redshift, consistent with our findings, though large error bars blur the trend. Their results were shown as probability density functions of  $m_1$  across redshift bins, which are normalized by the total number of events, a very uncertain quantity. As a result, error bars end up broadening. This issue is avoided when working with the volumetric merger rate. The counterpart limitation is that the non-overlap of confidence bands of the volumetric differential rate at different redshifts is not, by itself, sufficient to establish redshift evolution of the mass distribution, as discussed above. Finally, unlike the binned method, our interpolation points are data-driven rather than fixed, potentially capturing finer features by construction.

### 3. ASTROPHYSICAL INTERPRETATION

We now turn to the astrophysical interpretation of our results. Metal-rich stars experience enhanced mass loss through stellar winds and produce lighter compact remnants. Consequently, the chemical enrichment of the Universe over cosmic time is expected result in lighter (heavier) BBHs at lower (higher) redshifts. Several population-synthesis studies have indeed predicted an evolution of the BBH mass spectrum with redshift (see e.g. Mapelli et al. 2019; Neijssel et al. 2019; van Son et al. 2022b; de Sá et al. 2024).

Our triangulation-based reconstruction suggests that the known feature in the BBH mass spectrum at  $M_{\text{tot}} \sim 70 M_{\odot}$ ,  $m_1 \sim 35 M_{\odot}$  is primarily due to mergers at  $z \gtrsim 0.7$ . There are at least three plausible, non-mutually exclusive explanations for such a high- $z$  excess:

- (i) Pulsational pair-instability supernovae (PPISN) has long been invoked to explain a pileup of masses at the instability onset. Recent studies, however, have been indicating that this interpretation is in conflict with both theoretical predictions of the location of the mass gap (Farag et al. 2022; Hendriks et al. 2023) as well as the relative number of systems within this mass range (Stevenson et al. 2019). A rapid rotation of stellar progenitors before core collapse could, in principle, align the PPISN pile up with the feature

observed in GW data (Winch et al. 2025). The prevalence of such a mass peak at  $z \gtrsim 0.7$  could then be interpreted as the evolution of the PPISN mass scale with redshift due to a combination of the mild effect of progenitor metallicity on the maximum BH mass (Farmer et al. 2019) and the distribution of time delays between zero-age-main-sequence and that of the BBH merger (Mukherjee 2022).

- (ii) The internal structure of massive stars before core collapse might also play an important role in determining peaks in the BBH mass distribution. Schneider et al. (2021, 2023) showed that stellar-origin BHs with  $m_1 \gtrsim 30$  are produced by stars whose stellar structures have not been altered by binary interactions, with lower metallicities favoring higher masses. On the other hand, a star at (sub)solar metallicity stripped of its outer envelope results into a BH with typical mass  $m_1 \lesssim 10 M_{\odot}$  ( $m_1 \lesssim 20 M_{\odot}$ ). Under such considerations, the isolated evolution formation channel, which leads to stripped binaries, cannot explain the presence of a peak around  $m_1 \sim 35 M_{\odot}$  in the primary mass distribution of merging BBHs. This peak would then come from BHs formed from the collapse of single stars at low metallicities and later paired by other processes. This mechanism would introduce a difference in BH formation at masses similar to those inferred in this work, with a connection to stellar metallicity, hence redshift. That said, more work needs to be done to assess the compatibility of those models with our results.
- (iii) As for BBH formation in dense stellar clusters, N-body simulations that consistently include stellar evolution and binary interactions find that dynamically assembled GW sources are, on average, more massive than those from isolated evolution (Rodriguez et al. 2016; Di Carlo et al. 2019; Sedda et al. 2024). Dynamical formation has thus been identified as a plausible origin of the  $\sim 35 M_{\odot}$  primary-mass feature (Antonini et al. 2023; Bruel et al. 2025). Massive, dense globular clusters likely tend to form at earlier cosmic times with respect to the global formation of stars in the Universe (Choksi et al. 2018; El-Badry et al. 2019). This implies the globular cluster channel naturally predicts a high-mass contribution to the BBH merger rate that switches off at low redshifts. Previous explorations of this interplay predict a high-mass BBH peak at  $z \gtrsim 2$  that extends to lower redshifts (Ye & Fishbach 2024; Torniamenti et al. 2024), suggesting that our observation could correspond to the lower-redshift tail of this peak.

In addition, let us briefly comment on the lower-mass peak at  $M_{\text{tot}} \sim 20 M_{\odot}$ , which is present in our reconstruction at  $z = 0.2$  (uncertainties are too high to confirm its presence at  $z = 1$ ). This finding is consistent with the  $m_1 \sim 10 M_{\odot}$  peak already reported in several studies before ours (e.g. Abbott et al. 2021, 2023b; Abac et al. 2025b). Detailed binary-evolution calculations based on MESA (Paxton et al. 2011) reproduce a primary-mass peak around  $\sim 10 M_{\odot}$  at near-solar metallicity (Fragos et al. 2023; Agrawal et al. 2023). Isolated binaries evolving through stable mass transfer well match the low-mass end of the merging BBH population (van Son et al. 2022a). Our work is consistent with these results, but further observations are needed to confirm the invariance of the low-mass peak across redshift. The dynamical evolution of stars and compact objects in metal-rich dense clusters is also a plausible explanation (Ye et al. 2025).

#### 4. CONCLUSIONS

We presented a non-parametric reconstruction of the mass-redshift correlation in merging BBH using Delaunay triangulation and barycentric interpolation. Our analysis of GWTC-4.0 data reveals that the high-mass peak at  $M_{\text{tot}} \sim 70 M_{\odot}$  appears predominantly from  $z \gtrsim 0.7$  and is absent at  $z = 0.2$ .

So, where would the heavy binaries have gone? While a detailed comparison with astrophysical predictions is necessary, interpreting our results will require models in which BBH sub-populations contribute to the observed merger rate at different epochs, possibly shaped by the combined influence of stellar evolution, metallicity-dependent mass loss, and the relative importance of dynamical formation channels.

Moreover, our findings imply that analyses measuring cosmological parameters from the redshift dependence of the detector-frame mass spectrum (Chernoff & Finn 1993; Markovic 1993; Farr et al. 2019; Mastrogiovanni et al. 2021; Abac et al. 2025a) should carefully account for the evolution of the prominence of the high-mass peak with  $z$ .

Our findings suggest a correlation between BBH mass and merger redshift in GWTC-4.0 data. At the same

time, we caution against overinterpreting (the medians of) non-parametric reconstructions, which often, including here, come with large statistical errors.

The key strength of using Delaunay triangulation is that the interpolation skeleton, including the number and location of the nodes, is inferred directly from the data. In practice, this optimized complexity reduces the number of parameters by one to two orders of magnitude compared to the pixelized approach by Heinzel et al. (2025), and attain a good recovery of arbitrary functional forms at a lower tuning cost compared to the binned Gaussian-process approach by Ray et al. (2023), both of which rely on a fixed grid. For this reason, we expect our flexible framework to be significantly more efficient at probing correlations in dimensions  $\geq 3$  (as we will illustrate in an upcoming publication; Toubiana et al. 2025a), making it ideally suited for the forthcoming big-data era of GW astronomy.

#### ACKNOWLEDGEMENTS

We thank April Qiu Cheng, Raffi Enfiaud, Jack Heinzel, and Matthew Mould for discussions. R.T., A.T., T.B. and D.G. ERC Starting Grant No. 945155–GWmining, Cariplò Foundation Grant No. 2021-0555, MUR PRIN Grant No. 2022-Z9X4XS, Italian-French University (UIF/UF) Grant No. 2025-C3-386, MUR Grant “Progetto Dipartimenti di Eccellenza 2023-2027” (BiCoQ), and the ICSC National Research Centre funded by NextGenerationEU. A.T. and D.G. are supported by MUR Young Researchers Grant No. SOE2024-0000125. D.G. is supported by MSCA Fellowship No. 101149270–ProtoBH. Computational work was performed at CINECA with allocations through INFN and the University of Milano-Bicocca, and at NVIDIA with allocations through the Academic Grant program. This research has made use of data or software obtained from the Gravitational Wave Open Science Center.

*Software:* astropy (Robitaille et al. 2013), elyn (Karnesis et al. 2023), numpy (Harris et al. 2020), qhull (Barber et al. 1996), scipy (Virtanen et al. 2020).

#### REFERENCES

Abac, A. G., et al. 2025a, , arXiv:2509.04348 [astro-ph.CO]  
 —. 2025b, arXiv:2508.18083 [astro-ph.HE]  
 —. 2025c, arXiv:2508.18082 [gr-qc]  
 Abbott, B. P., et al. 2019, Phys. Rev. X, 9, 031040, arXiv:1811.12907 [astro-ph.HE]  
 Abbott, R., et al. 2021, Phys. Rev. X, 11, 021053, arXiv:2010.14527 [gr-qc]

Abbott, R., Abbott, T. D., Abraham, S., et al. 2021, *Astrophys. J. Lett.*, 913, L7, arXiv:2010.14533 [astro-ph.HE]  
 Abbott, R., et al. 2021, *Astrophys. J. Lett.*, 913, L7, arXiv:2010.14533 [astro-ph.HE]  
 —. 2023a, *Phys. Rev. X*, 13, 041039, arXiv:2111.03606 [gr-qc]

—. 2023b, *Phys. Rev. X*, 13, 011048, arXiv:2111.03634 [astro-ph.HE]

—. 2024, *Phys. Rev. D*, 109, 022001, arXiv:2108.01045 [gr-qc]

Adamcewicz, C., & Thrane, E. 2022, *Mon. Not. R. Astron. Soc.*, 517, 3928, arXiv:2208.03405 [astro-ph.HE]

Agrawal, P., Hurley, J., Stevenson, S., et al. 2023, *Mon. Not. R. Astron. Soc.*, 525, 933, arXiv:2303.10187 [astro-ph.SR]

Antonini, F., Gieles, M., Dosopoulou, F., & Chattopadhyay, D. 2023, *Mon. Not. R. Astron. Soc.*, 522, 466, arXiv:2208.01081 [astro-ph.HE]

Barber, C. B., Dobkin, D. P., & Huhdanpaa, H. 1996, *ACM Trans. Math. Software*, 22, 469

Biscoveanu, S., Callister, T. A., Haster, C.-J., et al. 2022, *Astrophys. J. Lett.*, 932, L19, arXiv:2204.01578 [astro-ph.HE]

Broekgaarden, F. S., Berger, E., Neijssel, C. J., et al. 2021, *Mon. Not. R. Astron. Soc.*, 508, 5028, arXiv:2103.02608 [astro-ph.HE]

Bruel, T., Lamberts, A., Rodriguez, C. L., et al. 2025, arXiv:2503.03810 [astro-ph.GA]

Callister, T. A. 2024, arXiv:2410.19145 [astro-ph.HE]

Chernoff, D. F., & Finn, L. S. 1993, *Astrophys. J. Lett.*, 411, L5, arXiv:gr-qc/9304020

Choksi, N., Gnedin, O. Y., & Li, H. 2018, *Mon. Not. R. Astron. Soc.*, 480, 2343, arXiv:1801.03515 [astro-ph.GA]

de Sá, L. M., Rocha, L. S., Bernardo, A., Bachega, R. R. A., & Horvath, J. E. 2024, *Mon. Not. R. Astron. Soc.*, 535, 2041, arXiv:2410.01451 [astro-ph.HE]

Delaunay, B. 1934, Bulletin de l'Académie des Sciences de l'URSS. Classe des sciences mathématiques et naturelles, 6, 793

Di Carlo, U. N., Giacobbo, N., Mapelli, M., et al. 2019, *Mon. Not. R. Astron. Soc.*, 487, 2947, arXiv:1901.00863 [astro-ph.HE]

El-Badry, K., Quataert, E., Weisz, D. R., Choksi, N., & Boylan-Kolchin, M. 2019, *Mon. Not. R. Astron. Soc.*, 482, 4528, arXiv:1805.03652 [astro-ph.GA]

Essick, R., & Fishbach, M. 2024, *Astrophys. J.*, 962, 169, arXiv:2310.02017 [gr-qc]

Essick, R., et al. 2025, arXiv:2508.10638 [gr-qc]

Farag, E., Renzo, M., Farmer, R., Chidester, M. T., & Timmes, F. X. 2022, *Astrophys. J.*, 937, 112, arXiv:2208.09624 [astro-ph.HE]

Farmer, R., Renzo, M., de Mink, S. E., Marchant, P., & Justham, S. 2019, *Astrophys. J.*, 887, 53, arXiv:1910.12874 [astro-ph.SR]

Farr, W. M., Fishbach, M., Ye, J., & Holz, D. 2019, *Astrophys. J. Lett.*, 883, L42, arXiv:1908.09084 [astro-ph.CO]

Fragos, T., et al. 2023, *Astrophys. J. Supp. S.*, 264, 45, arXiv:2202.05892 [astro-ph.SR]

Gennari, V., Mastrogiovanni, S., Tamanini, N., Marsat, S., & Pierra, G. 2025, *Phys. Rev. D*, 111, 123046, arXiv:2502.20445 [gr-qc]

Gerosa, D., & Fishbach, M. 2021, *Nat. Astron.*, 5, 749, arXiv:2105.03439 [astro-ph.HE]

Harris, C. R., et al. 2020, *Nature*, 585, 357, arXiv:2006.10256 [cs.MS]

Heinzel, J., Mould, M., & Vitale, S. 2025, *Phys. Rev. D*, 111, L061305, arXiv:2406.16844 [astro-ph.HE]

Hendriks, D. D., van Son, L. A. C., Renzo, M., Izzard, R. G., & Farmer, R. 2023, *Mon. Not. R. Astron. Soc.*, 526, 4130, arXiv:2309.09339 [astro-ph.HE]

Karnesis, N., Katz, M. L., Korsakova, N., Gair, J. R., & Stergioulas, N. 2023, *Mon. Not. R. Astron. Soc.*, 526, 4814, arXiv:2303.02164 [astro-ph.IM]

Kullback, S., & Leibler, R. A. 1951, *Ann. Math. Stat.*, 22, 79

Lalleman, M., Turbang, K., Callister, T., & van Remortel, N. 2025, *Astron. Astrophys.*, 698, A85, arXiv:2501.10295 [astro-ph.HE]

Mandel, I., & Farmer, A. 2022, *Phys. Rep.*, 955, 1, arXiv:1806.05820 [astro-ph.HE]

Mandel, I., Farr, W. M., & Gair, J. R. 2019, *Mon. Not. R. Astron. Soc.*, 486, 1086, arXiv:1809.02063 [physics.data-an]

Mapelli, M. 2021, in *Handbook of Gravitational Wave Astronomy* (Springer), arXiv:2106.00699 [astro-ph.HE]

Mapelli, M., Bouffanais, Y., Santoliquido, F., Sedda, M. A., & Artale, M. C. 2022, *Mon. Not. Roy. Astron. Soc.*, 511, 5797, arXiv:2109.06222 [astro-ph.HE]

Mapelli, M., Giacobbo, N., Santoliquido, F., & Artale, M. C. 2019, *Mon. Not. R. Astron. Soc.*, 487, 2, arXiv:1902.01419 [astro-ph.HE]

Markovic, D. 1993, *Phys. Rev. D*, 48, 4738

Mastrogiovanni, S., Leyde, K., Karathanasis, C., et al. 2021, *Phys. Rev. D*, 104, 062009, arXiv:2103.14663 [gr-qc]

Mukherjee, S. 2022, *Mon. Not. R. Astron. Soc.*, 515, 5495, arXiv:2112.10256 [astro-ph.CO]

Neijssel, C. J., Vigna-Gómez, A., Stevenson, S., et al. 2019, *Mon. Not. R. Astron. Soc.*, 490, 3740, arXiv:1906.08136 [astro-ph.SR]

Paxton, B., Bildsten, L., Dotter, A., et al. 2011, *Astrophys. J. Supp. S.*, 192, 3, arXiv:1009.1622 [astro-ph.SR]

Rajan, V. T. 1994, *Discrete Comput. Geom.*, 12, 189

Ray, A., Magaña Hernandez, I., Mohite, S., Creighton, J., & Kapadia, S. 2023, *Astrophys. J.*, 957, 37, arXiv:2304.08046 [gr-qc]

Rinaldi, S., Del Pozzo, W., Mapelli, M., Lorenzo-Medina, A., & Dent, T. 2024, *Astron. Astrophys.*, 684, A204, arXiv:2310.03074 [astro-ph.HE]

Rippa, S. 1990, *Comput. Aided Geom. Des.*, 7, 489

Robitaille, T. P., et al. 2013, *Astron. Astrophys.*, 558, A33, [arXiv:1307.6212 \[astro-ph.IM\]](https://arxiv.org/abs/1307.6212)

Rodriguez, C. L., Chatterjee, S., & Rasio, F. A. 2016, *Phys. Rev. D*, 93, 084029, [arXiv:1602.02444 \[astro-ph.HE\]](https://arxiv.org/abs/1602.02444)

Sadiq, J., Dent, T., & Lorenzo-Medina, A. 2025, [arXiv:2502.06451 \[gr-qc\]](https://arxiv.org/abs/2502.06451)

Schneider, F. R. N., Podsiadlowski, P., & Laplace, E. 2023, *Astrophys. J. Lett.*, 950, L9, [arXiv:2305.02380 \[astro-ph.HE\]](https://arxiv.org/abs/2305.02380)

Schneider, F. R. N., Podsiadlowski, P., & Müller, B. 2021, *Astron. Astrophys.*, 645, A5, [arXiv:2008.08599 \[astro-ph.SR\]](https://arxiv.org/abs/2008.08599)

Sedda, M. A., Kamlah, A. W. H., Spurzem, R., et al. 2024, *Mon. Not. R. Astron. Soc.*, 528, 5140, [arXiv:2307.04807 \[astro-ph.HE\]](https://arxiv.org/abs/2307.04807)

Sedda, M. A., Mapelli, M., Benacquista, M., & Spera, M. 2023, *Mon. Not. R. Astron. Soc.*, 520, 5259, [arXiv:2109.12119 \[astro-ph.GA\]](https://arxiv.org/abs/2109.12119)

Stevenson, S., Sampson, M., Powell, J., et al. 2019, *Astrophys. J.*, 882, 121, [arXiv:1904.02821 \[astro-ph.HE\]](https://arxiv.org/abs/1904.02821)

Talbot, C., & Golomb, J. 2023, *Mon. Not. R. Astron. Soc.*, 526, 3495, [arXiv:2304.06138 \[astro-ph.IM\]](https://arxiv.org/abs/2304.06138)

Torniamenti, S., Mapelli, M., Périgois, C., et al. 2024, *Astron. Astrophys.*, 688, A148, [arXiv:2401.14837 \[astro-ph.HE\]](https://arxiv.org/abs/2401.14837)

Toubiana, A., Katz, M. L., & Gair, J. R. 2023, *Mon. Not. R. Astron. Soc.*, 524, 5844, [arXiv:2305.08909 \[gr-qc\]](https://arxiv.org/abs/2305.08909)

Toubiana, A., Tenorio, R., Bruel, T., Gerosa, D., & Gair, J. R. 2025a, in preparation

Toubiana, A., et al. 2025b, [arXiv:2507.13249 \[gr-qc\]](https://arxiv.org/abs/2507.13249)

van Son, L. A. C., de Mink, S. E., Renzo, M., et al. 2022a, *Astrophys. J.*, 940, 184, [arXiv:2209.13609 \[astro-ph.HE\]](https://arxiv.org/abs/2209.13609)

van Son, L. A. C., de Mink, S. E., Callister, T., et al. 2022b, *Astrophys. J.*, 931, 17, [arXiv:2110.01634 \[astro-ph.HE\]](https://arxiv.org/abs/2110.01634)

Virtanen, P., et al. 2020, *Nat. Methods*, 17, 261, [arXiv:1907.10121 \[cs.MS\]](https://arxiv.org/abs/1907.10121)

Vitale, S., Gerosa, D., Farr, W. M., & Taylor, S. R. 2020, in *Handbook of Gravitational Wave Astronomy* (Springer), [arXiv:2007.05579 \[astro-ph.IM\]](https://arxiv.org/abs/2007.05579)

Winch, E. R. J., Sabhahit, G. N., Vink, J. S., & Higgins, E. R. 2025, *Mon. Not. R. Astron. Soc.*, 540, 90, [arXiv:2504.17009 \[astro-ph.SR\]](https://arxiv.org/abs/2504.17009)

Ye, C. S., & Fishbach, M. 2024, *Astrophys. J.*, 967, 62, [arXiv:2402.12444 \[astro-ph.HE\]](https://arxiv.org/abs/2402.12444)

Ye, C. S., Fishbach, M., Kremer, K., & Reina-Campos, M. 2025, [arXiv:2507.07183 \[astro-ph.HE\]](https://arxiv.org/abs/2507.07183)

## APPENDIX

## A. DELAUNAY TRIANGULATION FOR INFERENCE

We seek to represent general multidimensional distributions using an agnostic model with a low computational cost. Our strategy is to construct a trans-dimensional interpolator for the merger rate using barycentric interpolation on a Delaunay triangulation (Delaunay 1934; Rippa 1990; Rajan 1994). The number of triangulation points is allowed to vary through inference, thus modeling arbitrarily simple (or complex) distributions depending on the available information in the data. This method can be applied to parameter spaces of arbitrary dimensionality. While we restrict our application of the method to a two-dimensional parameter space, we describe it in full generality.

We model the differential number of events  $d_\theta N(\theta; \Lambda)$  in dimension  $D$ . The hyperparameters  $\Lambda$  we aim to infer are the number of triangulation vertices  $N_v$ , their locations  $v_k$ , and their weights  $w_k$ , where the  $v_k$ 's live in the same space as  $\theta$  and the  $w_k$ 's are real numbers.

In our current implementation, we infer the rate within a  $D$ -dimensional box  $\mathcal{D}$  so that  $d_\theta N(\theta) = 0$  if  $\theta \notin \mathcal{D}$ . To do so, we place  $N_c = 2^D$  fixed vertices at the corners of the domain; their associated weights  $\{W_k, k = 1, \dots, N_c\}$  are allowed to vary. Thus,

$$\Lambda = \left\{ N_v, \{W_k\}_{k=1, \dots, N_c}, \{v_k, w_k\}_{k=1, \dots, N_v - N_c} \right\}. \quad (\text{A1})$$

The number of free parameters is

$$N_{\text{par}} = 1 + N_c + (D + 1)(N_v - N_c) = 1 - D 2^D + (D + 1)N_v. \quad (\text{A2})$$

We denote the (natural log) differential rate as computed by a triangulation with parameters  $\Lambda$  by  $\log d_\theta N(\theta|\Lambda) \equiv \Delta(\theta|\Lambda)$ . To compute the differential rate at a given point  $\theta$ , we find the simplex  $S(\theta)$  (i.e. triangle if  $D = 2$ ) wherein it lies, compute its barycentric coordinates, and use them to linearly interpolate the weights at their vertices.

$$\Delta(\theta|\Lambda) = \sum_{v \in S(\theta)} w_v b_v(\theta). \quad (\text{A3})$$

We illustrate this process for  $D = 2$  in Fig. 1. In such case, each triangle  $S(\theta)$  has three pairs of vertices and weights  $\{(v_1, w_1), (v_2, w_2), (v_3, w_3)\}$  from which one can construct three barycentric coordinates  $\{b_1(\theta), b_2(\theta), b_3(\theta)\}$ .

The number of expected events within a domain  $\mathcal{D}$  for a given triangulation  $\Lambda$  is given by

$$N(\Lambda; \mathcal{D}) = \int_{\theta \in \mathcal{D}} d\theta e^{\Delta(\theta|\Lambda)}. \quad (\text{A4})$$

For a single simplex  $S$ , Eq. (A4) can be expressed in closed form as

$$N(\Lambda; S) = D! |S| \sum_{i=1}^{D+1} \frac{\exp(w_i)}{\prod_{j \neq i} (w_i - w_j)}, \quad (\text{A5})$$

where  $|S|$  denotes the generalized volume of  $S$  (i.e. the area if  $D = 2$ ) and  $w_{1, \dots, D+1}$  are the weights of its vertices.

We construct Delaunay triangulations using `qhull` (Barber et al. 1996) via `scipy` (Virtanen et al. 2020).

## B. FORMALISM FOR HIERARCHICAL INFERENCE

We express the population likelihood for observing  $N_{\text{obs}}$  events with data  $\{d_j\} = \{d_1, \dots, d_{N_{\text{obs}}}\}$  for a set of population hyperparameters  $\Lambda$  as (Mandel et al. 2019; Vitale et al. 2020)

$$p(\{d_j\}|\Lambda) \propto e^{-N_{\text{det}}(\Lambda)} \prod_{j=1}^{N_{\text{obs}}} \left\langle \frac{d_\theta N(\theta|\Lambda)}{\pi_{\text{PE}}(\theta)} \right\rangle_{\theta \sim p(\theta|d_j)}, \quad (\text{B6})$$

where  $p(\theta|d_j)$  and  $\pi_{\text{PE}}(\theta)$  are the posterior and prior distribution of the parameters describing event  $j$ . The number of expected events  $N_{\text{det}}(\Lambda)$  is given by

$$N_{\text{det}}(\Lambda) = \left\langle \frac{d_\theta N(\theta|\Lambda)}{\pi_{\text{inj}}(\theta)} p(\text{det}|\theta) \right\rangle_{\theta \sim \pi_{\text{inj}}(\theta)} \quad (\text{B7})$$

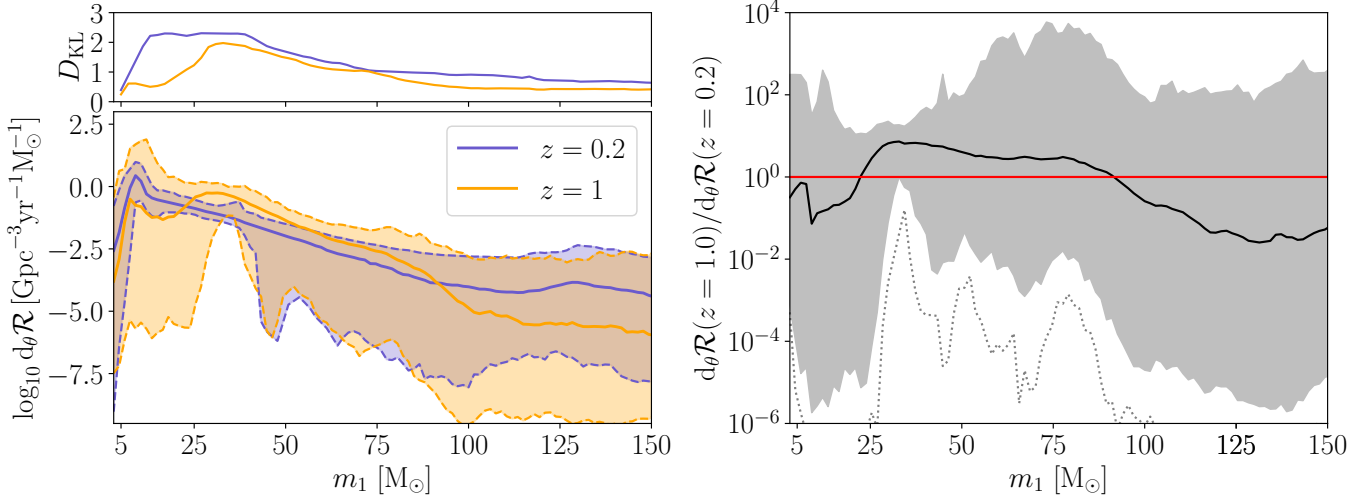


**Figure 4.** Joint reconstruction of the  $(m_1, z)$  BBH volumetric merger rate, mirroring Fig. 2 in the main body of the paper. A constant rate is excluded with 95% credibility (i.e. the solid red line is included in the 90% symmetric credible interval, here shaded in grey).

where

$$p(\text{det}|\theta) = \int_{d > \text{threshold}} p(d|\theta) \, dd, \quad (\text{B8})$$

is the probability of detecting a source with parameters  $\theta$ ,  $p(d|\theta)$  is the likelihood for data  $d$ , and the integral is restricted to realizations  $d$  that exceed the detection threshold (defined via the chosen ranking statistic).

Equations (B6) and (B7) are computed via Monte Carlo integration, here indicated with  $\langle \cdot \rangle$ . Selection effects are estimated using the injection campaign presented by [Essick et al. \(2025\)](#). We set the population likelihood to zero for hyperparameters that yield a variance in the Monte Carlo estimators greater than one ([Talbot & Golomb 2023](#); [Abac et al. 2025b](#)).

For cosmological calculations, we assume the `Planck15` cosmology as implemented in `astropy` ([Robitaille et al. 2013](#)).

### C. POPULATION INFERENCE FOR $(m_1, z)$

To facilitate comparison with other studies, Fig. 4 shows the results of our method applied to the joint  $(m_1, z)$  distribution instead of  $(M_{\text{tot}}, z)$ . The significance of the enhanced rate at  $\sim 35 M_{\odot}$  at  $z = 1$  versus  $z = 0.2$  is slightly lower than for  $(M_{\text{tot}}, z)$  (95% vs. 98.5%, right panel of Fig. 4), likely due to larger measurement uncertainties in  $m_1$ , but the qualitative disappearance of the high-mass peak at low redshift persists.